

# A Prediction Scheme for Loader Excavation Resistance Based on Parallel Hybrid Deep Neural Network

Yingnan Li<sup>ID</sup>, Student Member, IEEE, Shunshun Zhang<sup>ID</sup>, Guanlong Chen<sup>ID</sup>, Zongwei Yao<sup>ID</sup>, Qiushi Bi<sup>ID</sup>, and Xuefei Li<sup>ID</sup>

**Abstract**—In response to the challenge of directly measuring excavation resistance, this study introduces a predictive method based on a parallel hybrid deep neural network. Initially, addressing the difficulty in obtaining excavation resistance data, a joint electromechanical-hydraulic simulation model for loaders was developed to generate a dataset for excavation resistance. Considering the presence of local spatial features and long-term dependencies in the sequence, a residual structure was incorporated into the convolutional neural network (CNN) to enhance the focus on significant features in the resistance data during spatial feature extraction. Additionally, gated recurrent units (GRUs) were employed to capture temporal features. Subsequently, these two types of features were separately unfolded and then integrated through a fully connected layer to facilitate feature fusion, thereby avoiding the degradation of original data features typical in traditional serial architectures. Finally, the predictive performance of the proposed method was evaluated in comparative experiments with CNNs, GRUs, Transformers, and serial-structure hybrid neural networks. The results demonstrated an improvement in prediction accuracy compared to other methods. Specifically, the weighted mean absolute percentage error (WMAPE) values for longitudinal resistance ( $F_x$ ), vertical resistance ( $F_z$ ), and resistance torque ( $M_y$ ) were 2.89%, 3.5%, and 5.78%, respectively. The proposed method decreases the WMAPE by 45.47%, 44.35%, and 26.8% in comparison to the serial architecture. The mean  $R^2$  values were 0.982, 0.977, and 0.962, respectively.

**Index Terms**—Deep learning, excavation resistance, feature fusion, multisourced data.

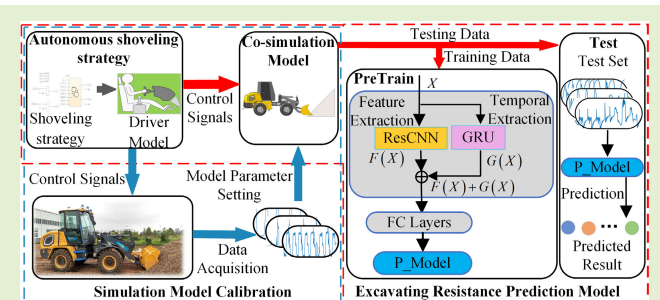
## I. INTRODUCTION

LOADERS, as primary transportation vehicles in fields such as mining, ports, and mixing stations, directly influence the productivity of overall operations [1]. Among these, autonomous shoveling represents a crucial element in realizing independent loader operation. The real-time adjustment of shoveling strategies based on excavation resistance is essential for enhancing shoveling efficiency [2], [3]. However, obtaining precise material information beforehand to determine excavation resistance remains a challenging task [4]. Moreover, since excavation resistance arises from complex interactions

Received 14 April 2025; revised 6 June 2025; accepted 6 June 2025. Date of publication 16 June 2025; date of current version 16 July 2025. This work was supported by the National Natural Science Foundation of China under Grant 52372428, Grant 52375246, and Grant 52105100. The associate editor coordinating the review of this article and approving it for publication was Dr. Xu Cheng. (Corresponding authors: Qiushi Bi; Xuefei Li.)

The authors are with the Key Laboratory of CNC Equipment Reliability, Ministry of Education, School of Mechanical and Aerospace Engineering, Jilin University, Changchun 130022, China (e-mail: lyn\_jlu@163.com; s18840653969@163.com; chengl22@mails.jlu.edu.cn; yzw@jlu.edu.cn; bqs@jlu.edu.cn; lixuefeijlu@163.com).

Digital Object Identifier 10.1109/JSEN.2025.3578306



between the material and the bucket, directly measuring this resistance via sensors is particularly problematic [5]. Consequently, the main motivation and key contribution of this article is the design of a parallel hybrid neural network architecture to realize real-time prediction of excavation resistance, based on indirectly obtainable operational parameters from loaders.

Extensive research has been conducted on estimating loader excavation resistance based on traditional approaches. Zhao et al. [6] introduced a fuzzy estimation strategy during the penetration process to estimate soil characteristic parameters in real time. Building on this, their team improved the finite-element equation (FEE) model to predict soil resistance. Furthermore, Madau et al. [7] established dynamic and kinematic models at the front end of the loader's working device and then calculated the horizontal and vertical forces applied at the bucket's center of gravity using a free-body diagram. Bi et al. [8] applied kinematic modeling and static analysis to an electric shovel, using a torque balance function to estimate the static effective load online. Wang et al. [9] conducted static analysis on a loader bucket to determine the collection points for indirect forces and fit

it with strain gauges to measure the indirect forces arising from digging resistance in real time. Gao et al. [10] established a longitudinal dynamic model of the digging process and combined it with singular value decomposition unscented Kalman filter (SVDUKF) algorithm to estimate the longitudinal excavation resistance during the penetration process.

As far as current scholarship is aware, several challenges persist in the methodologies employed for acquiring digging resistance. First, methods based on the FEE encounter difficulties in parameter identification when applied to wheel loaders operating with mixed-material loads of unknown properties. Second, static analysis methods are primarily suited for static estimations of load in the bucket. Third, methods that measure digging resistance indirectly through the installation of strain gauges are limited by calibration precision and are not suitable for large-scale integrated installations. Lastly, solutions based on state estimation algorithms can fail due to inaccuracies in constructing the physical model.

To address these issues, scholars have proposed integrating neural networks with empirical formulas to mitigate prediction biases caused by inaccurate material parameters. Wei et al. [11] have suggested calibrating material parameters using a backpropagation neural network (BPNN). Li et al. [12] have evaluated the performance of a physical information machine learning approach that integrates mechanistic models for modeling digging resistance. In efforts to enhance the accuracy of external force estimations, Shen et al. [13] designed a Gaussian process regression (GPR) model to compensate for errors in the rigid body dynamics (RBD) model. However, as loaders often operate with a mixture of various materials, the generalizability of these solutions is compromised. Consequently, Wu et al. [14] have implemented a soft sensing of loader working resistance using a random forest regression algorithm optimized via grid search. Huo et al. [15] used an RBF neural network for predicting the hydraulic cylinder load in excavators. Chen et al. [16] applied a particle swarm optimization (PSO) algorithm to optimize hyperparameters in a long short-term memory (LSTM) network, enhancing prediction accuracy. An analysis of the literature reveals that prior studies have predominantly focused on the long-term temporal dependencies present in digging resistance data. However, the local spatial characteristics associated with transient shocks or changes in resistance due to tire slippage during the digging process have received little attention, failing previous solutions under certain conditions.

In the predictive modeling of excavation resistance in loaders, the excavation conditions demonstrate significant non-linear characteristics, which often lead to slow convergence and entrapment in local minima when employing BPNNs and radial basis function neural networks (RBFNNs) [17]. Convolutional neural networks (CNNs), as a quintessential feedforward neural network, utilize unique convolutional and pooling operations to effectively learn latent features within excavation data. Moreover, if solely CNNs are employed for the extraction of spatial features of digging resistance, a deeper network architecture is necessitated to address the nonlinearity in the prediction process. However, research indicates that beyond a certain network depth, performance tends to saturate

and may even decline. In light of these issues, He et al. [18] proposed a residual network that transfers low-level features directly to higher levels, thereby achieving improved training outcomes.

Regarding the temporal features present in sequential data, recurrent neural networks (RNNs) enhance the processing capabilities for such data by adding connections between the neurons in the hidden layers. Harrou et al. [19] combined the benefits of wavelet denoising and RNNs to attain precise traffic flow forecasting. Hittawe et al. [20] devised an innovative stacked architecture named StackPred, which markedly enhanced the predictive accuracy of sea surface temperature and wind speed utilizing Transformers. Consequently, several scholars have suggested the serial integration of networks such as LSTM and gated recurrent units (GRUs) within CNN architectures [21], [22]. Although such hybrid methods have achieved commendable performance to some extent, the initial spatial feature extraction via the CNN network, followed by transmission through a smoothing layer to the GRU network for temporal feature extraction, leads to the smoothing out of locally extracted spatial features and disrupts the long-term dependencies present in the original data. To overcome this drawback, a parallel CNN-LSTM cooperative spectrum sensing scheme was designed [23], which enhances the model's predictive capabilities through two independent feature extraction channels.

Based on the aforementioned analysis, the primary contributions of this study are summarized as follows.

- 1) Addressing the challenge of directly and precisely extracting resistance data during the excavation process in real vehicles. This study developed a comprehensive electromechanical-hydraulic material joint simulation model and calibrated the model parameters using real vehicle data to obtain a more accurate model for acquiring excavation operation data.
- 2) A novel PaHDNN model for predicting the excavation resistance of loaders was proposed. This framework not only enhances the capability of extracting local spatial features present in the excavation resistance data but also overcomes the mutual interference encountered by traditional serial hybrid neural networks in perceiving different data features, thereby facilitating an improvement in the accuracy of predicting excavation resistance in loaders.
- 3) In contrast to existing studies, the methodology proposed in this research does not require precise physical models and material parameters. It applies to the complex and variable conditions encountered in loader excavation operations, providing technical support for developing autonomous loading strategies and allocating excavation power.

The organization of the article is as follows. Section II analyzes the force process during loader excavation operations and introduces a predictive framework for excavation resistance. Section III describes our simulation model and validates it through real-vehicle experiments. Section IV introduces the Pa HDNN model. In Section V, validation experiments based on simulation data are presented and compared with traditional methods. Section VI summarizes our research.

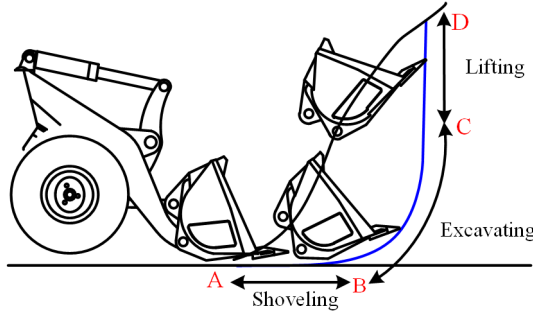


Fig. 1. Division of excavation stages for loaders.

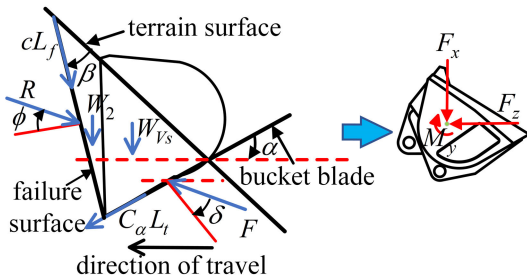


Fig. 2. Loader excavation force.

## II. BACKGROUND

As shown in Fig. 1, the digging action can be divided into three stages based on the bucket action [24]: the shoveling stage, the excavating stage, and the lifting stage. In the shoveling stage (AB section), the bucket enters the material pile at a certain angle until the bucket cuts into a certain depth; this stage is mainly subject to longitudinal resistance. Then, in the excavating stage (BC section), the boom cylinder and the bucket cylinder are operated to cut and load the material into the bucket. Due to the interaction between the material and the bucket, the main force position and direction during this stage change with the bucket attitude. Finally, during the lifting stage (CD section), the loading task of the material is completed by lifting the boom; this stage is mainly affected by the gravitational force of the material.

Referring to the basic earthwork equation [25], the loader is subjected to the excavating resistance shown in Fig. 2 during the digging operation, where  $F$  represents the sum of the frictional resistance between the bottom of the bucket and the material,  $C_\alpha L_t$  represents the resistance along the cutting edge direction,  $R$  is the total resistance of external materials to the bucket when the bucket moves forward,  $cL_f$  is the force between the bucket and the sliding surface,  $W_{Vs}$  represents the total gravitational force of the material in the bucket, and  $W_2$  represents the gravitational force of the material from the cutting part of the bucket during the cutting motion.

From Fig. 2, these forces change in magnitude, direction, and position as the bucket moves in the material pile during the operation of the loader [26]. These parameters are difficult to accurately measure in an actual excavation, causing difficulty in obtaining the excavation resistance of loaders. To simplify the model in this study, the force acting on the shovel is translated to the center of mass of the bucket itself, and the longitudinal shovel resistance  $F_x$  and vertical shovel resistance  $F_z$  are obtained. Then, by introducing an additional resistance

moment  $M_y$ , the influence of the position changes of the force is corrected [25].

## III. MODEL VALIDATION AND DATA ACQUISITION

The excavating operation of loaders is a complex nonlinear and discontinuous process, causing difficulty in directly establishing accurate mathematical models to describe the process [27], [28], [29]. Therefore, an integrated co-simulation system of “machine electricity hydraulic control material” is established, as shown in Fig. 3, and models the entire loading operation process of the loader. The principle of co-simulation is that the vehicle dynamics module in RecurDyn receives the information, such as wheel torque and hydraulic pressure from the transmission and hydraulic systems, drives the motion of the vehicle’s walking system and working device, and completes the interaction between the bucket and the discrete element module. The excavating resistance experienced by the bucket is then fed back to the control, transmission, and hydraulic systems through the vehicle dynamics module. To ensure smooth reading, the key parameters of the loader are added in Tables I–IV.

### A. Model Validation

*1) Design of the Experimental Equipment and Working Conditions:* The experimental platform is based on the Type 18 electric loader, as shown in Fig. 4. This experimental platform includes a vehicle controller (NBC301-10 controller) and a CAN communication device (CANalyst II baud rate: 250 Kbs) for collecting onboard information (torque and speed of the walking motor). In addition, oil pressure sensors [SUNBUN high-precision oil pressure sensor, accuracy  $\leq 0.5\%$  (F.S.)] and angle sensors [CONTALEC angle sensor, accuracy  $\leq 0.3\%$  (F.S.)] were installed at the positions of the boom cylinder and the bucket cylinder of the experimental vehicle to obtain pressure and displacement information of the rod cavity and rodless cavity of the cylinder. RTK and IMU were installed above the driver to collect vehicle speed and position information. Finally, all information is integrated into the vehicle CAN bus, and all data are recorded in real time in the data terminal unit (DTU).

To ensure the effectiveness of the training data, three experiments were designed to verify the accuracy of the simulation model. The experimental conditions are designed as follows.

- 1) A climbing experiment is used to verify the accuracy of the power system and transmission system. The experimental conditions are designed as follows: a slope of 18% is set on the cement road surface, and the loader starts from a flat area close to the slope. When the rear wheels reach the slope, the driver presses the accelerator pedal to the maximum opening, and the loader begins to accelerate and then climbs at a constant speed until the uphill process ends.
- 2) The movement experiment of the working device is used to verify the accuracy of the kinematics model of the working device and the hydraulic system. The specific working conditions are set as follows: on a flat cement road surface, the loader is kept in a stationary state, and the rapid movement of the working device is completed by operating the hydraulic pilot handle. The action sequence is to flip the bucket upward. When the

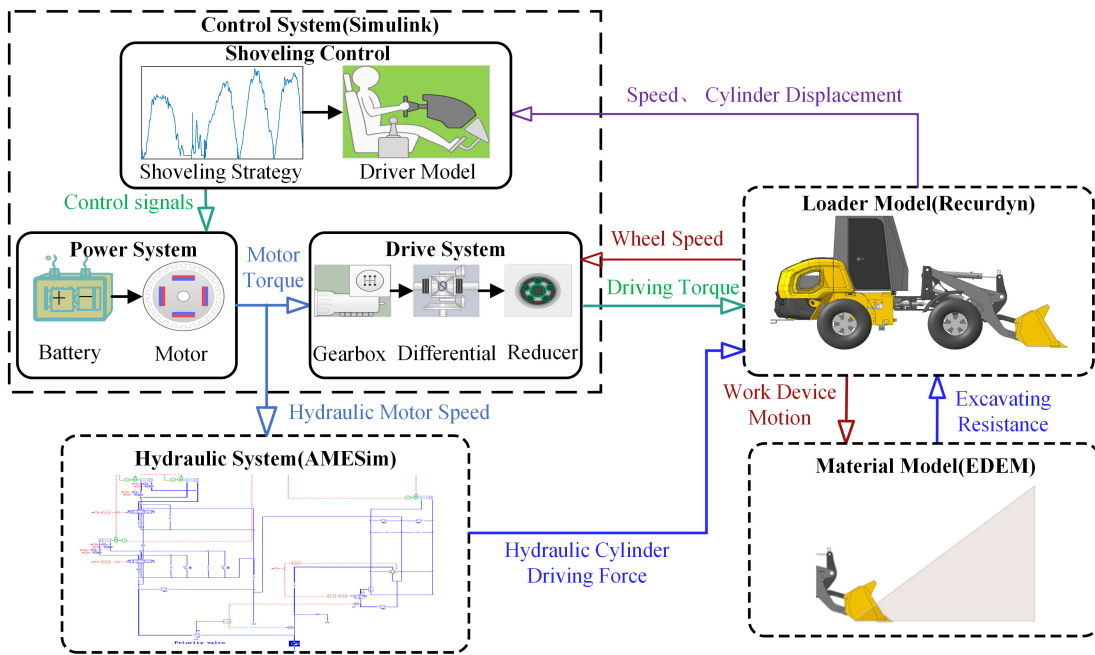


Fig. 3. Loader co-simulation model.



Fig. 4. Experimental equipment and operating conditions.

- bucket touches the limit block, the boom is lifted to the limit position, the bucket is flipped downward, and finally, the boom is lowered to the initial position.
- 3) The shoveling experiment verifies the accuracy of the discrete element model and the resistance of the working device. The experimental conditions are as follows: the loader operates on limestone, and during this process, the boom cylinder remains stationary. At moment 0, the loader is stationary, and the speed of the vehicle is 0,

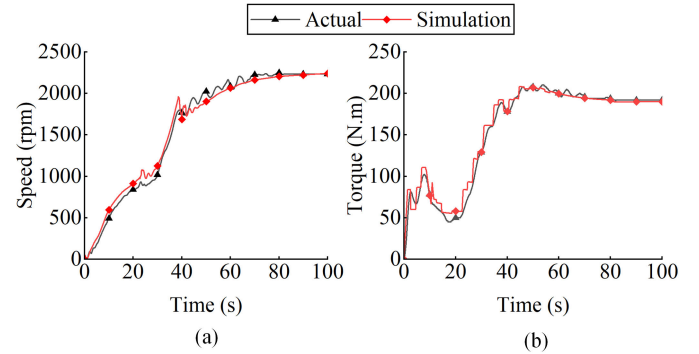


Fig. 5. Comparison results of the climbing experiment. (a) Speed comparison result. (b) Torque comparison result.

with the bucket flat and attached to the ground. After the excavation begins, the vehicle speed gradually increases until it enters the material pile. Due to the resistance of the material, the vehicle begins to slow down. When the desired full bucket rate is reached, the accelerator pedal is released and the bucket is flipped upward.

**2) Climbing Experiment:** Since an electric loader is used, the speed and torque of the walking motor are key indicators for measuring the power characteristics of the entire vehicle.

By comparing the simulation results and experimental results of the two, as shown in Fig. 5, the trend and magnitude of the speed and torque characteristics of the walking motor in the simulation environment are highly consistent with the experimental data, confirming the accuracy of the power system model constructed in our study. Furthermore, this article utilizes widely accepted model evaluation metrics, including mean absolute error (MAE), root-mean-square error (RMSE), and coefficient of determination ( $R^2$ ), to reflect the model's accuracy. The comparative results of the climbing experiment are detailed in Table V.

**TABLE I**  
LOADER STRUCTURE PARAMETERS

Parameter	Value	Parameter	Value
Loader quality/kg	6770	Wheel spacing/m	2.15
Bucket capacity/ $m^3$	1	Bucket width/m	1.982
Tire radius/m	0.53	Rated load/t	1.8

**TABLE II**  
MOTOR PARAMETERS

	Peak/Rated power(kW)	Peak/Rated torque(Nm)	Peak/Rated speed(r/min)	DC(V)
Walking motor	72/40	600/333	5000/1420	540
Hydraulic motor	45/24	170/91.7	3000/2500	540

**TABLE III**  
HYDRAULIC COMPONENT PARAMETERS

Hydraulic Component	Parameter	Value
Boom cylinder	Cylinder diameter/mm	85
	Rod diameter/mm	50
	Stroke/mm	545
Bucket cylinder	Cylinder diameter/mm	100
	Rod diameter/mm	50
	Stroke/mm	295
Hydraulic pump	Rated pressure/MPa	25
	Rated speed/rpm	2500
	Theoretical displacement/mL.r <sup>-1</sup>	38
Relief valve	Valve pressure/MPa	24

**TABLE IV**  
MATERIAL PARAMETERS

Value	Material			
	Sand	Limestone	Corn	Coal
Density/kg.m <sup>-3</sup>	2368	2612	1197	2178
Shear modulus/MPa	44.8	10	9.3	17.5
Poisson's ratio	0.36	0.25	0.4	0.23
Recovery Coefficient of material	0.43	0.55	0.25	0.5
Coefficient of static friction of material	0.57	0.2	0.09	0.6
Coefficient of rolling friction of material	0	0.2	0	0.05
Recovery Coefficient of material and bucket	0.2	0.5	0.9	0.5
Coefficient of static friction of material and bucket	0.15	0.7	0.22	0.3
Coefficient of rolling friction of material and bucket	0.01	0.15	0	0.05

**3) Action Experiment on the Working Device in Place:** In this experiment, a scheme using hydraulic pump speed and directional valve opening as inputs is used to complete the driving process of the working device in the simulation model. The actual and simulation experimental results are shown in Fig. 6, and the two subgraphs show the experimental and simulation data of the boom angle and bucket angle. As shown in the figure, the error between the motion of the simulation model and the measured data is relatively low throughout the entire experimental process.

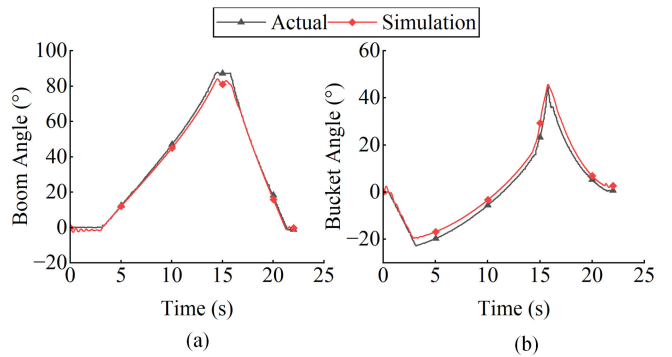


**Fig. 6.** Comparison results of the working device angle. (a) Boom angle comparison result. (b) Bucket angle comparison result.

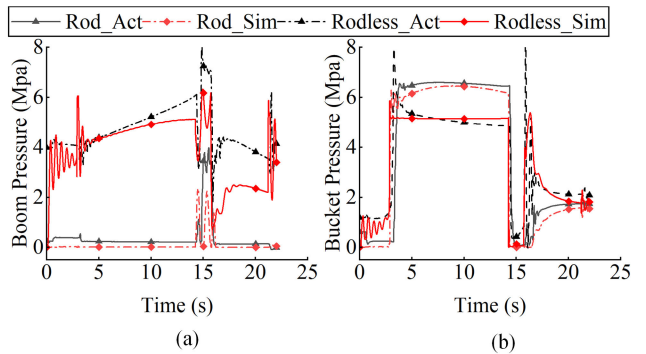


**Fig. 7.** Comparison results of the working equipment pressure. (a) Boom pressure comparison result. (b) Bucket pressure comparison result.

**TABLE V**  
EVALUATION RESULTS OF THE CLIMBING EXPERIMENT

Index	MAE	RMSE	$R^2$
Motor Speed	58.62r/min	71.11r/min	0.99
Motor Torque	5.29N.m	8.00N.m	0.98

From Fig. 7, the experimental and simulation data of the cylinder pressure during the process of bucket up tilting, boom lifting, and bucket overturning show good consistency. The pressure fluctuation in the initial stage of simulation is relatively large because the tire model needs to calculate the contact with the road surface in the early stage of simulation, generating vibration of the entire vehicle and affecting the hydraulic cylinder pressure. Second, during the boom lowering stage, there is a significant difference between the measured and simulated data of the rodless chamber pressure of the boom cylinder, which is potentially caused by inaccurate valve port area data. Because the research object is the excavation operation process of the loader and the lowering action of the boom is not involved in this process, the impact of the model errors in this section of the research results is disregarded.

The specific evaluation results of the work device model are presented in Table VI. It is important to note that due to significant pressure deviations of the boom cylinder during the descent process, the  $R^2$  value cannot accurately reflect the fitting degree between the boom cylinder simulation model and the actual model. Therefore, the  $R^2$  value for the boom cylinder is not provided.

In summary, our established working device model has similar characteristics to the actual vehicle and can meet the

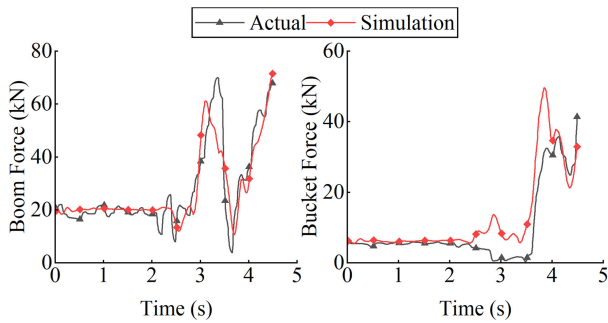


**Fig. 8.** Comparison of the shovel excavation experiment and simulation results.

**TABLE VI**  
EVALUATION RESULTS OF THE CYLINDER MOTION EXPERIMENT

Index	MAE	RMSE	$R^2$
Boom Angle	1.68°	2.16°	0.99
Lift Angle	2.62°	2.91°	0.96
Boom Rod Pressure	0.51MPa	0.75MPa	\
Boom Rodless Pressure	0.48MPa	0.74MPa	\
Bucket Rod Pressure	1.21MPa	1.46MPa	0.73
Bucket Rodless Pressure	0.45MPa	0.94MPa	0.74

accuracy requirements of the hydraulic model for the research content of our study.

**4) Excavation Operation Experiment:** To achieve the goal of restoring the effect of the bucket on the material pile, a strategy of excavating discrete element materials using a multibody dynamic model driven by experimentally measured loader motion data (walking motor speed and bucket cylinder angle) is used in a virtual simulation.

The comparison between the simulation and experimental results is shown in Fig. 8. During the loading phase (2.3–3.7 s), to ensure that the bucket does not damage the previously leveled road surface, a certain gap must be maintained between the bucket and the ground. This results in the material at the bottom of the bucket exerting a resistance force on the cylinder, and the variability in the flowability of the material causes differences in the forces experienced during this phase. After the insertion is completed, the loader stops moving forward. Due to the decrease in wheel drive force, the force on the boom cylinder also decreases and reaches its lowest point at approximately 3.5 s. Subsequently, the bucket cylinder begins to retract the bucket, and the force curves of the boom and bucket cylinder increase simultaneously.

As shown in the model evaluation results in Table VII, the experimental data and simulation data have similar patterns, verifying the rationality of using the discrete element model to simulate the excavation effect of the loader on loose materials.

### B. Data Acquisition

**1) Feature Selection:** It is well known that excavation data are influenced by numerous factors [14]. Consequently, the selection of appropriate training inputs is crucial for the convergence and accuracy of predictions. In recent years, the maximal information coefficient (MIC) has been extensively employed to identify strong nonlinear relationships between features [30]. An MIC-related heatmap, as shown in Fig. 9, quantifies the correlation between excavation resistance and the selected features. Three groups of excavation resistance

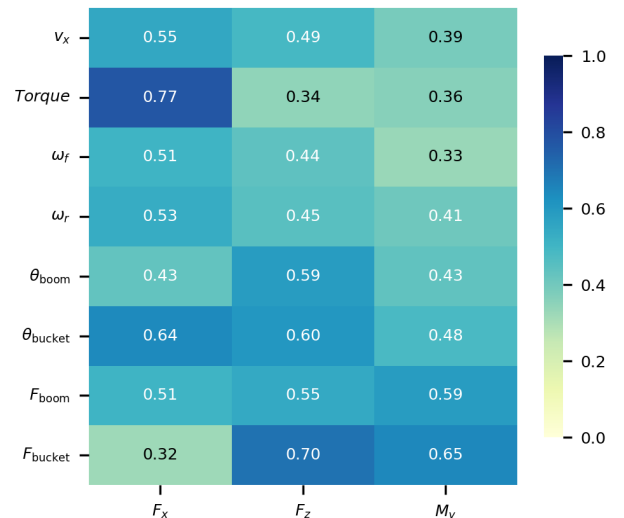


**Fig. 9.** MIC heatmaps of selected features.

**TABLE VII**  
EVALUATION RESULTS OF THE SHOVELING EXPERIMENT

Index	MAE	RMSE	$R^2$
Boom Cylinder Force	5.09kN	7.34kN	0.85
Bucket Cylinder Force	3.94kN	6.00kN	0.83

sequences exhibit distinct correlations with external features, owing to their complex variation patterns. In the longitudinal resistance sequence, the main influencing factors are the longitudinal forces exerted by the wheels, primarily correlated with the driving motor torque, vehicle speed, and the velocities of the front and rear tires. For the vertical resistance sequence, the force balance equation reveals stronger correlations between the posture of the working device and the forces on the hydraulic cylinders. Typically, an MIC value below 0.4 indicates a weak correlation. Despite some features having an MIC value slightly below 0.4 with a single sequence, the proposed input features in this study adequately consider the differences between various resistance sequences, as evidenced by the overall correlations shown in Fig. 9.

**2) Dataset:** In general, the physical qualities of materials result in varying excavation resistance [31]. Depending on how hard the excavation was, corn, sand, and limestone were chosen as the loader's working materials to improve the model's ability to generalize and make accurate predictions. Because noise is common in the real world, Gaussian noise was added to the simulation model to match the sensor error range seen in the real vehicle data collection system. The mean and variance of the pressure signal are 0 and 0.0044, respectively, whereas the mean and variance of the angle signal are 0 and 0.021, respectively. Each operational cycle lasts approximately 5–6 s, relying on the complexity of mining various materials and the evolution of mining strategies. We collected a total of around 11 000 data points at a sample frequency of 100 Hz, which formed the dataset for the predictive model. The dataset's statistical description is presented in Table VIII.

The input data of vehicle speed, walking motor torque, front and rear wheel speeds, and working device angles can be directly extracted from the RecurDyn software, while

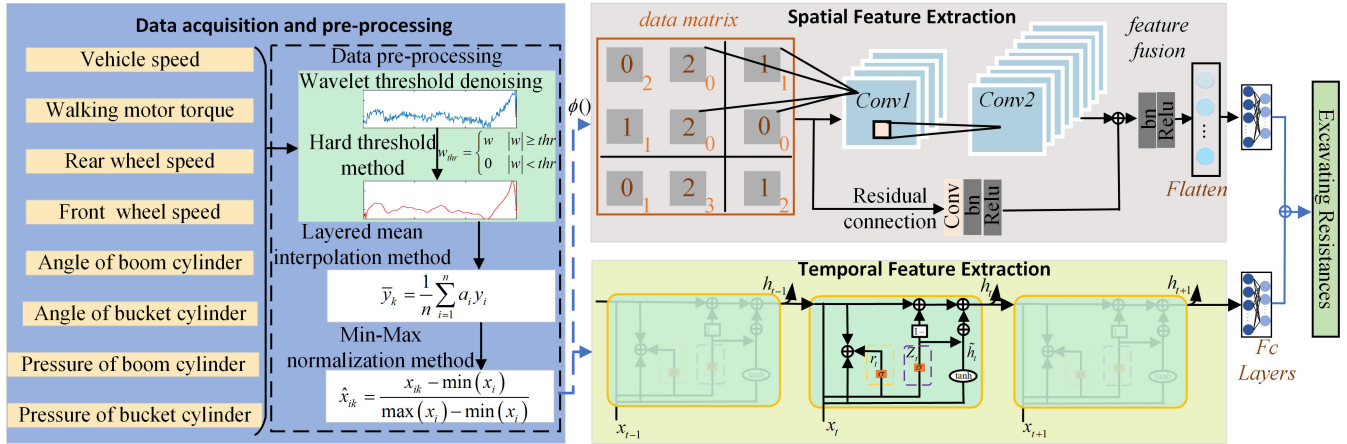


Fig. 10. PaHDNN network structure.

TABLE VIII  
STATISTICAL DESCRIPTION OF THE DATASET

	Count	Mean	Std	Min	50%	Max
$v_x$	10989	0.306	0.38504	0	0.136	1.77
Torque	10989	106.8	87.51359	0	92.91	267
$\omega_f$	10989	1.638	13.178	-8.62	0.481	380
$\omega_r$	10989	0.659	0.86984	-3.47	0.36492	8.833
$\theta_{boom}$	10989	56.53	2.72288	1.76	58.19735	58.69
$\theta_{bucket}$	10989	43.79	10.73574	1.64	49.30282	51.38
$F_{boom}$	10989	80.53	37.70011	-4.74	81.982	156.42
$F_{bucket}$	10989	29.52	27.13663	-33.18	33.19166	105.89

the working device cylinder pressure information is obtained through AMESim. Due to the interaction between the bucket and the material in the EDEM, the EDEM applies the force between the material and the force between the bucket and the material, that is, the excavating resistance experienced by the loader during the digging process, to the center of mass of the bucket and transmits it to the virtual prototype of the loader through the bucket. Therefore, as the output data of the training model, the excavating resistance can be obtained via the RecuDyn software. In practical applications, the mentioned input information can be obtained through sensors mounted on the loader as detailed in Section III-A.

#### IV. METHOD

To enhance excavation resistance prediction, we calibrate the coupled simulation model in Section III using real-world vehicle data to generate a diverse and reliable training dataset. Subsequently, in this section, the dataset undergoes preprocessing, followed by the training of the resistance prediction model using the proposed PaHDNN neural network framework.

##### A. PaHDNN Network Structure

In our study, a PaHDNN network was used to accurately predict the excavating resistance during loader operation. The structure of the proposed resistance prediction model is shown in Fig. 10. It encompasses three key components: data preprocessing, spatial feature extraction, and temporal feature extraction. Here, the following provides a brief description of each part.

###### 1) Data Preprocessing:

Due to the challenging working conditions of the loader and the influence of data collection conditions, raw

data typically suffers from issues such as data noise, inconsistent data scales, and local extreme values. These challenges can significantly impact the construction and training outcomes of the network model. Therefore, this article employs commonly used methods for data preprocessing. First, wavelet threshold denoising is applied to effectively suppress high-frequency noise in the original excavation condition signals, while preserving important time-frequency features through the multiresolution characteristics of wavelet transforms [32]. Although no explicit time-frequency decomposition techniques (such as STFT, HHT, or VMD) are used in the model, wavelet-based denoising offers a lightweight and practical solution that implicitly captures relevant frequency components without introducing additional transformation steps. Second, to address the challenges of inconsistent data scales and missing values, a layered mean interpolation method is selected based on the temporal characteristics of excavation conditions [9]. Lastly, considering the nonuniform units in excavation condition data, the chosen normalization method is the min-max normalization approach [33].

- 2) *Spatial Feature Extraction*: Given the multitude of time-varying factors inherent in the excavation process, data typically demonstrates dynamic fluctuations, information richness, and strong coupling. To extract more profound and deeper-level feature information, this article treats excavation data as a single-channel image composed of a 2-D pixel matrix, employing two convolution operations for feature extraction. To mitigate the risk of vanishing gradients in convolutional networks, which could lead to a performance decline, the article introduces residual connections. Through this approach, original data features are directly propagated to higher layers of the network, ensuring the precision of data feature representation [34].
- 3) *Temporal Feature Extraction*: To efficiently extract temporal features from excavation condition data and predict excavation resistance, this article utilizes a three-layer GRU neural network [35]. Additionally, to prevent the model from overfitting, a Dropout layer is introduced after each GRU network

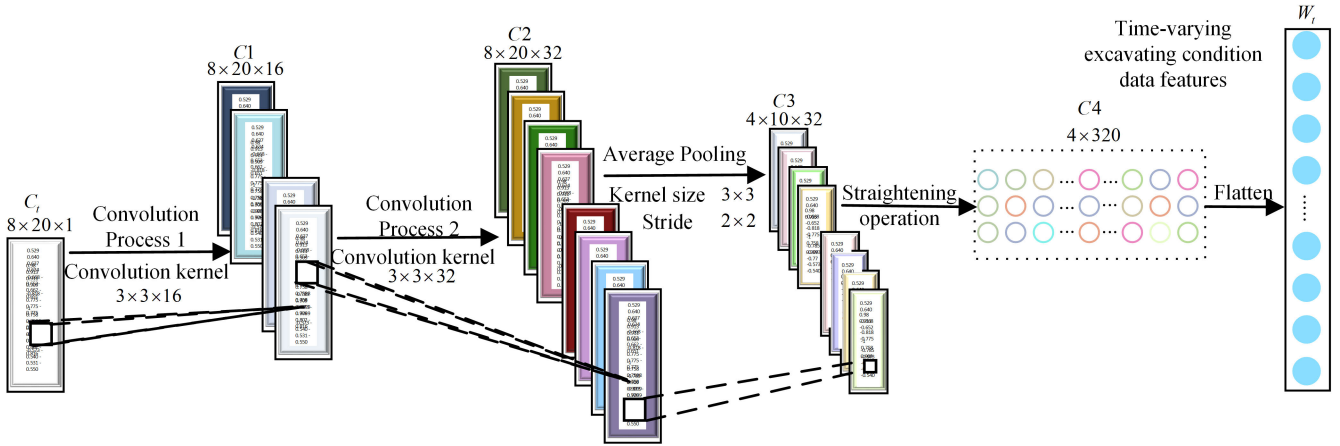


Fig. 11. CNN convolutional and pooling operations.

**TABLE IX**  
CNN NETWORK FEATURE EXTRACTION PROCESS

Input: Excavation condition data sample  $C_t$  at time  $t$ ;  
Output: Data feature vector  $W_t$

- Step 1: Performing operations such as interval sampling, prediction sample segmentation, and data normalization preprocessing on the original excavation condition data to obtain the data matrix  $C_t$  at time  $t$ ;
- Step 2: In the initial convolutional processing step, 16 convolutional kernels of size  $3 \times 3$  are applied to the data matrix  $C_t$ , yielding 16 new feature matrices of size  $8 \times 20$ . The trainable parameters of the convolutional kernels, the number of neurons in the conv1 layer, and the total connections are illustrated in Fig.11;
- Step 3: In the second convolutional processing step, 32 convolutional kernels of size  $3 \times 3$  are utilized to perform a secondary processing on the feature matrix extracted in step 2, resulting in 32 new feature matrices of size  $8 \times 20$ . This process involves a secondary extraction of deeper implicit features from the original data matrix;
- Step 4: To enhance computational efficiency, down-sampling is applied to the data in Step 3, employing average pooling with a window size of  $3 \times 3$  and a stride of  $2 \times 2$ . This process yields  $32 \times 4 \times 10$  feature matrices;
- Step 5: The 32 pooled feature matrices, each of size  $4 \times 10$ , are sequentially inserted into a  $4 \times 320$  data matrix;
- Step 6: The data matrix obtained in Step 5 serves as the input to the unfolding layer, with the excavation resistance data value at time  $t + 1$  as the label. Through the principles of backpropagation, the network model parameters are adjusted and updated, ultimately resulting in the feature vector  $W_t$  for the excavation condition data at time  $t$ .

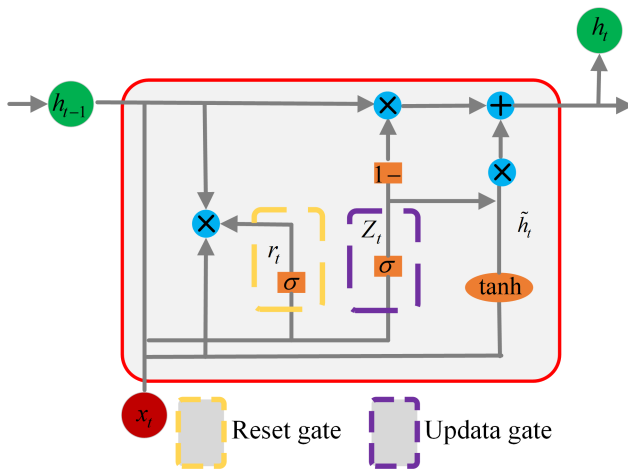


Fig. 12. GRU network structure.

layer. During the backpropagation process, the Adam algorithm is employed for gradient descent optimization.

### B. Convolutional Neural Network

In this article, the time-varying excavation condition data is treated as a single-channel pixel matrix image. Subsequently, adaptive feature extraction is performed using a CNN network

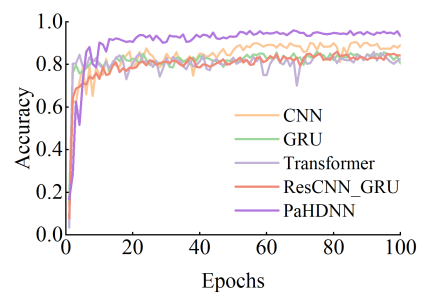


Fig. 13. Relationship between accuracy and number of iterations of different network models.

model, as illustrated in Fig. 11. Taking real-time operating parameters during the loader's excavation process (such as vehicle speed, walking motor torque, front and rear wheel speeds, angles of the boom cylinder and bucket cylinder, and pressures of the boom cylinder and bucket cylinder) as examples. The sampled data is collected at intervals of 0.2 s, forming an  $8 \times 20$  time-varying condition data matrix  $C_t$ . The specific feature extraction process is outlined in Table IX. To summarize temporal features after convolution, we apply a temporal average pooling layer in the ResCNN module. This approach is simple and efficient and helps reduce feature dimensionality while preserving important information.

**TABLE X**  
NETWORK TRAINING PARAMETERS

Parameter type	Setting
Epoch	100
Learning rate	0.01
Batch size	50
Loss function	MAE
Optimizer	Adam

**TABLE XI**  
PAHDNN LAYER STRUCTURE

	Layer	Filters	Kernel	Activation
CNN	Conv_2D	16	3*3	ReLU
	Conv_2D	32	3*3	ReLU
	Averagepooling	-	2*2	-
	Flatten	-	-	-
GRU	GRU	64	-	tanh
	GRU	32	-	tanh
	GRU	16	-	tanh

Compared with attention-based pooling, average pooling has better interpretability and lower complexity, which is more suitable for real-time excavation tasks. It avoids introducing extra parameters and makes the model more stable and easier to deploy in practical applications.

### C. Residual Neural Network

For example, if  $X_l$ ,  $W_l$ , and  $b_l$  are specified as the input, weight, and offset parameters of layer  $l$  ( $l = 1 \dots n$ ) for a multilayer neural network, respectively, then the gradient of the loss function is calculated as follows [36]:

$$\begin{aligned} & \frac{\partial \text{Loss}}{\partial W_1} \\ &= \frac{\partial \text{Loss}}{\partial F_n(X_n, W_n, b_n)} \times \frac{\partial F_n(X_n, W_n, b_n)}{\partial F_n(X_{n-1}, W_{n-1}, b_{n-1})} \\ & \quad \times \dots \times \frac{\partial F_2(X_2, W_2, b_2)}{\partial F_1(X_1, W_1, b_1)} \times \frac{\partial F_1(X_1, W_1, b_1)}{\partial W_1} \end{aligned} \quad (1)$$

where  $F_n(\cdot)$  is used to describe the nonlinear function of input and output. When the residual network is applied to a CNN, the gradient is changed to the following:

$$\frac{\partial X_{l+1}}{\partial X_l} = \frac{\partial H(X_l)}{\partial X_l} + \frac{\partial F(X_l, W_l, b_l)}{\partial X_l}. \quad (2)$$

In (2), function  $H(\cdot)$  is a mapping function of input  $X_l$ , which usually consists of a convolution function, identity function, that merely repeats the features of the low-level, rather than learning new features. Inspired by this, the residual neural network is introduced in the algorithm proposed in this article, to enhance the accuracy of excavation resistance prediction.

### D. Gate Recurrent Unit

As shown in Fig. 12, the memory block of the GRU typically includes an update gate  $z_t$  and a reset gate  $r_t$ .

In the GRU network structure, the input gate and forgetting gate in the LSTM network are combined to form an update

gate to control how much historical information needs to be neglected and how much new information needs to be received in the current state. The expressions for the update gate and the current hidden state are shown in the following equations:

$$z_t = \sigma(W_{zx}x_t + W_{zh}h_{t-1} + b_z) \quad (3)$$

$$h_t = z_t \tilde{h}_t + (1 - z_t) h_{t-1}. \quad (4)$$

$x_t$  and  $h_{t-1}$  represent the input vector at time  $t$  and the output of the memory block at time  $t - 1$ , respectively;  $W_{zx}$  and  $W_{zh}$  are the weight matrices of the input and hidden states to the update gate, respectively;  $b_z$  represents the bias;  $\sigma$  is the activation function of sigmoid; and  $\tilde{h}_t$  is the candidate hidden state.

From (5) and (6), the range of reset gate values is [0–1]. When the value is close to 1, the current state completely reads the historical state information. Similarly, when the value is close to 0, the current state completely disregards the historical state information. Therefore, the function of resetting the gate is to determine how much information in the candidate states is obtained from the historical information

$$r_t = \sigma(W_{rx}x_t + W_{rh}h_{t-1} + b_r) \quad (5)$$

$$\tilde{h}_t = \tanh(W_{hx}x_t + W_{hh}(r_t h_{t-1}) + b_h). \quad (6)$$

$W_{rx}$  and  $W_{rh}$  are the weight matrices of the input and hidden states to the reset gate, respectively;  $b_r$  represents the bias;  $W_{hx}$  and  $W_{hh}$  are the input and reset gate-adjusted hidden state to candidate hidden state weight matrices, respectively; and  $b_h$  represents the bias.

## V. RESULTS AND ANALYSIS

### A. Network Structure and Training Parameters

To ensure the effectiveness of the PaHDNN network model in predicting excavation resistance, this article utilizes grid search, guided by the experience of neural network parameter tuning, to select the optimal number of neurons and hyperparameter values. The training parameter settings are referenced in Table X, and the key network configuration parameters of PaHDNN are outlined in Table XI.

### B. Performance of Feature Fusion Networks

To analyze the effectiveness of the feature fusion network model constructed in this study, the dataset constructed in Section III-B was used to verify whether the improved fusion network structure can enhance the prediction performance of excavation resistance. Traditional prediction network models were compared in this study, namely: 1) CNN: using the CNN model alone; 2) GRU: using the GRU model alone; 3) Transformer: using the Transformer model alone; 4) ResCNN\_GRU: first extracting spatial features with the residual CNN model, then sequentially extracting temporal features with the GRU model; and 5) PaHDNN: CNN and GRU models separately extract their respective features, then fuse them in parallel. The relationship between the prediction accuracy and iteration times of the five networks is shown in Fig. 13.

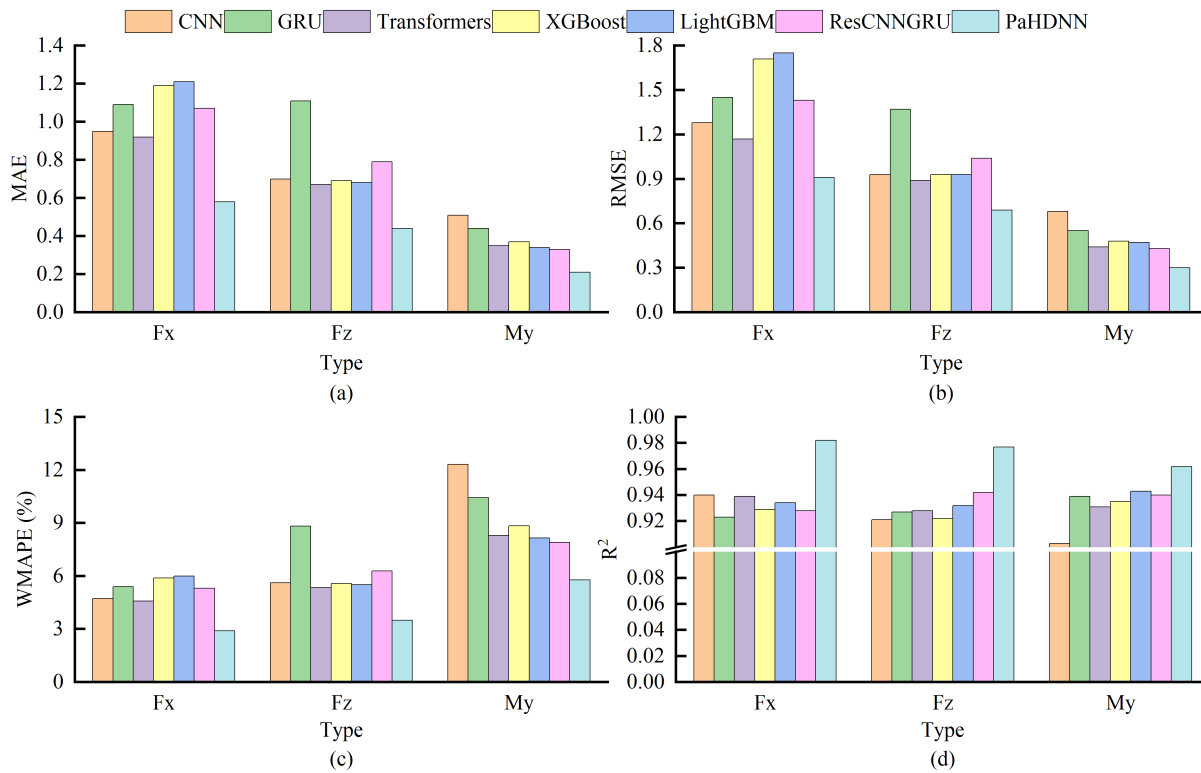


**Fig. 14.** Comparison of excavation resistance prediction models under different evaluation metrics. (a) MAE results. (b) RMSE results. (c) WMAPE results. (d)  $R^2$  results.

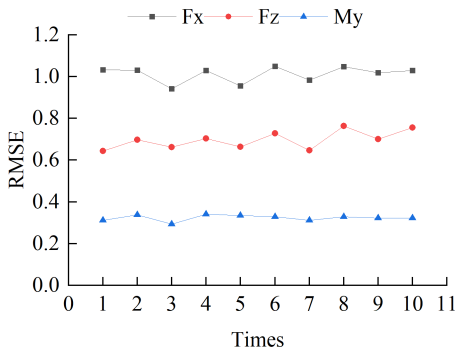


**Fig. 15.** RMSE values of ten  $k$ -fold experiments.

In this study, the following evaluation metrics were used: MAE, RMSE, weighted mean absolute percentage error (WMAPE), and coefficient of determination ( $R^2$ ). As shown in Fig. 14, PaHDNN exhibits strong advantages across all four dimensions. Under MAE evaluation, the PaHDNN neural network shows the lowest MAE, with Fx, Fz, and My values of 0.58 kN, 0.48 kN, and 0.21 kN·m, respectively. In the WMAPE and  $R^2$  evaluations, it was found that My had the worst model error percentage and goodness of fit among all the models. This is because during the excavation process, the rolling of material during collection causes the torque in the  $y$ -direction to fluctuate more significantly than the forces in the  $x$ - and  $z$ -directions, making it more difficult to predict. However, compared to the other models, the difference between PaHDNN is more similar. Among them, the MAPE of Fx and Fz is close, at approximately 3%, while the MAPE of My is slightly higher, at 5.78%. In terms of the  $R^2$  metric, Fx, Fz, and My achieved values of 0.982, 0.977, and 0.962, respectively, all demonstrating superior fitting performance.

It is imperative to develop a reliable excavation resistance prediction model with good consistency. To this end, we employed a  $k$ -fold cross-validation method with  $k = 10$  in our evaluation experiments [37]. The training set described in Section III-B was evenly divided into ten distinct subsets. Subsequently, each subset was used as a validation set in turn, with the remaining nine subsets serving as the training set, and this process was repeated ten times. The model evaluation outcomes, as depicted in Fig. 15, show the standard deviations of the RMSE across ten cycles of cross-validation to be 0.073, 0.053, and 0.014, respectively, indicating good consistency across the three training outputs.

### C. Predictive Performance for Different Materials

The characteristics of different materials can influence excavation resistance; therefore, this study examined three types of materials with varying excavation difficulties: sand, limestone, and corn. The predictive results for these materials are presented in Figs. 16–18. The figures illustrate that all five predictive models effectively estimated the digging resistance. The PaHDNN model, in particular, demonstrated superior fit and predictive accuracy. Observations of the predictive curves for the three materials revealed similar trends in excavation resistance for the same material, while distinct local features emerged due to differences in material properties. This underscores the necessity of constructing a feature fusion model

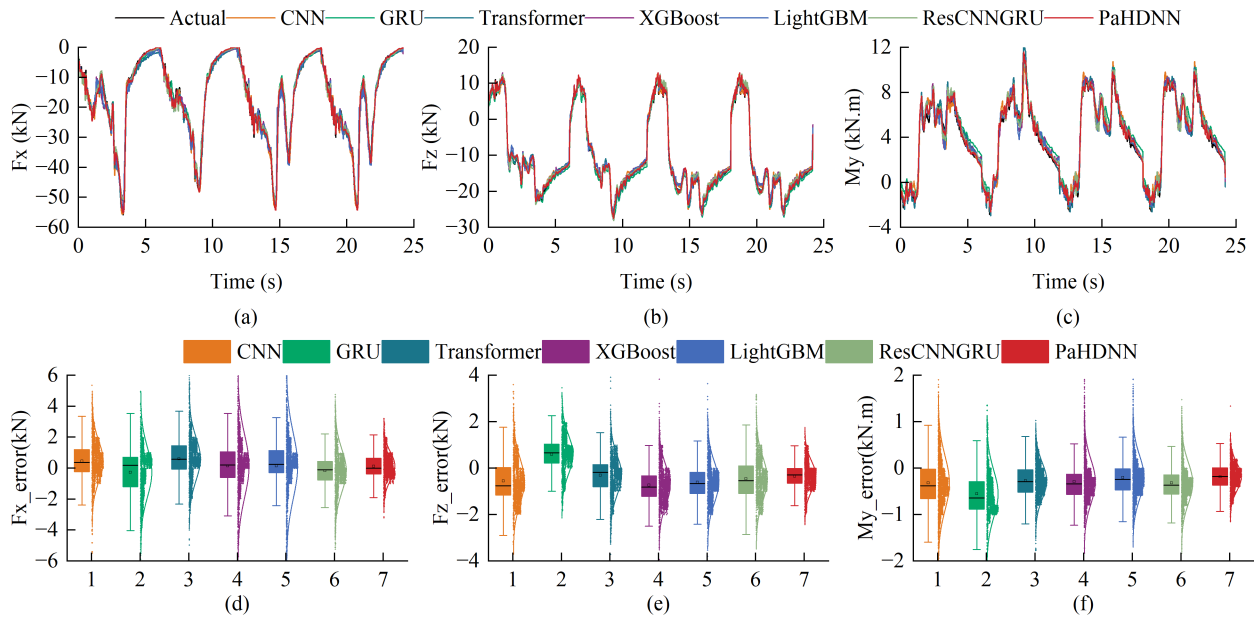


**Fig. 16.** Comparison of different model predictions in sand conditions. (a) Longitudinal resistance results. (b) Vertical resistance results. (c) Resistance torque result. (d) Longitudinal resistance errors distribution. (e) Vertical resistance errors distribution. (f) Resistance torque errors distribution.

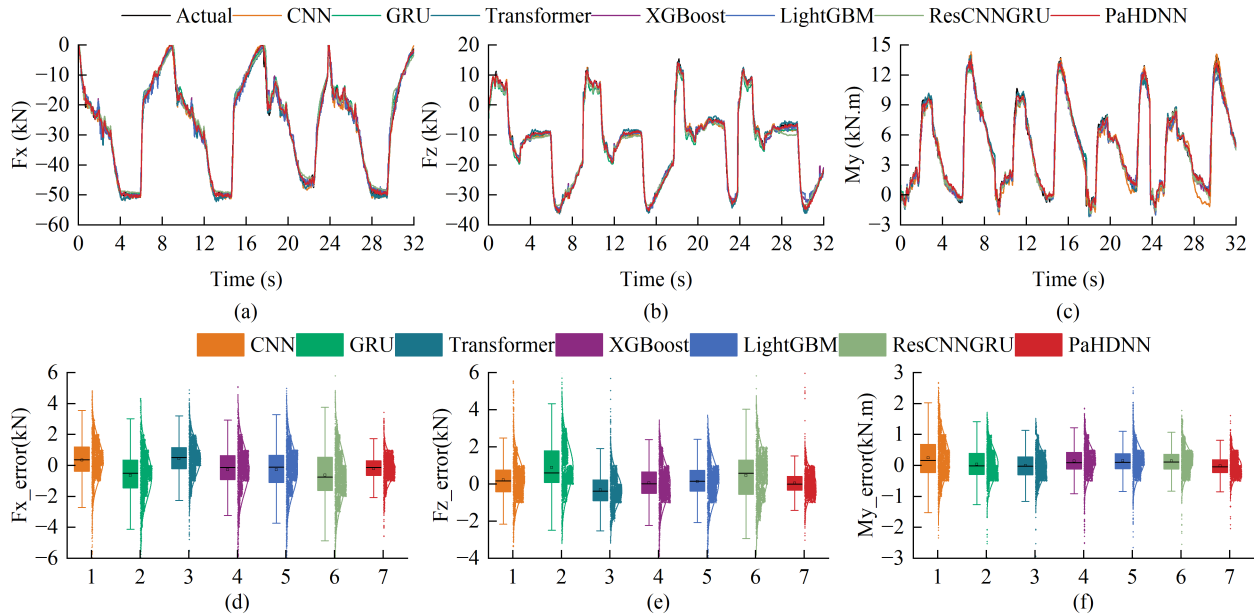


**Fig. 17.** Comparison of different model predictions in limestone conditions. (a) Longitudinal resistance results. (b) Vertical resistance results. (c) Resistance torque result. (d) Longitudinal resistance errors distribution. (e) Vertical resistance errors distribution. (f) Resistance torque errors distribution.

for loader excavation resistance that accounts for long-term dependencies and local characteristics. To visually demonstrate the predictive performance for different materials, (d)–(f) in Figs. 16–18 depict box plots of excavation resistance errors and the fit normal curves of these errors. Across all box plots, the PaHDNN model's boxes were more centralized and the medians were closer to zero compared to other models. Moreover, the error distribution fitting results for the three materials, as shown in Tables XII–XIV, indicate similar variances and means in the prediction errors for different materials, suggesting that the proposed approach effectively

addresses the limitations of existing models due to material properties.

Furthermore, to thoroughly assess the predictive performance of the PaHDNN model in relation to benchmark models, we performed a series of paired sample t-tests on the absolute prediction errors of all test samples. Table XV presents the statistical outcomes of various predictive measures. In every instance, the computed t-statistic is positive and the *p*-value is 0, signifying that the discrepancies in prediction errors between PaHDNN and their corresponding baselines are markedly significant.

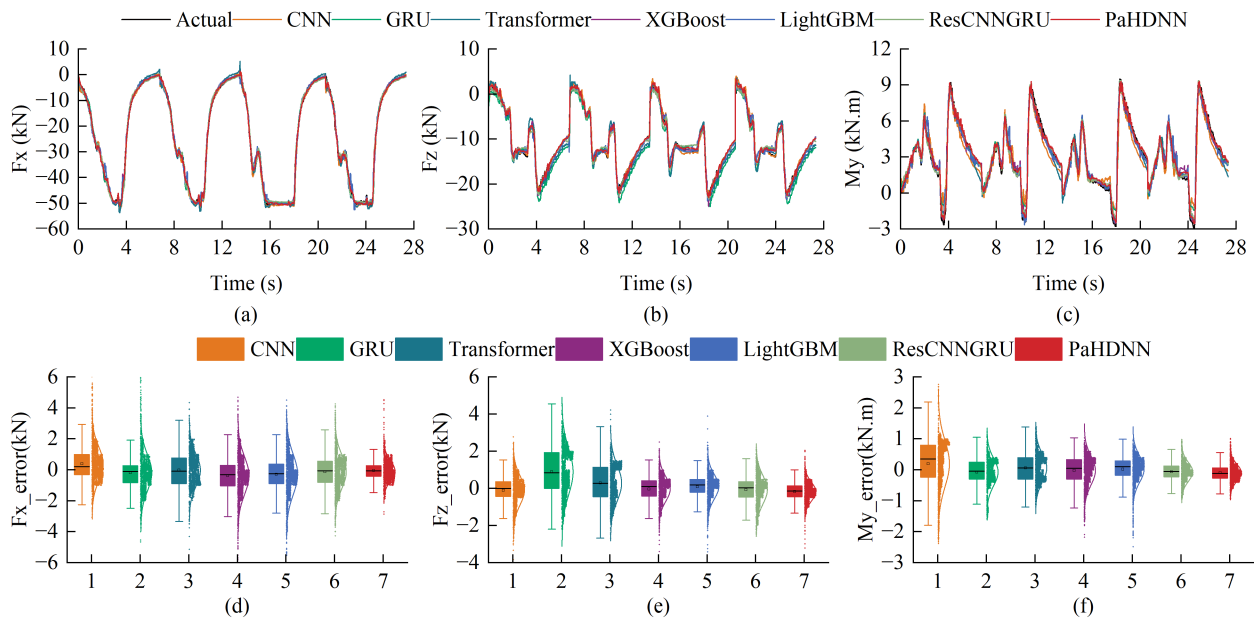


**Fig. 18.** Comparison of different model predictions in corn conditions. (a) Longitudinal resistance results. (b) Vertical resistance results. (c) Resistance torque result. (d) Longitudinal resistance errors distribution. (e) Vertical resistance errors distribution. (f) Resistance torque errors distribution.

TABLE XII  
DISTRIBUTION RESULTS OF PREDICTION ERRORS IN SAND CONDITIONS

	CNN	GRU	Transformer	XGBoost	LightGBM	ResCNNGRU	PaHDNN
$F_x$	$\mu$	0.448	-0.266	0.605	0.138	0.151	<b>-0.165</b>
	$\sigma$	1.308	1.603	1.391	2.015	2.111	<b>1.377</b>
	50%	0.366	0.192	0.578	0.208	0.251	-0.094
	$\mu$	-0.553	0.589	<b>-0.297</b>	-0.73	-0.614	-0.461
$F_z$	$\sigma$	0.97	0.821	0.84	0.859	0.885	<b>0.647</b>
	50%	-0.758	0.662	<b>-0.175</b>	-0.812	-0.659	-0.543
	$\mu$	-0.319	-0.551	-0.271	-0.289	-0.197	-0.319
	$\sigma$	0.584	0.511	0.384	0.471	0.462	<b>0.292</b>
$M_y$	50%	-0.381	-0.638	-0.292	-0.339	-0.239	-0.362
	$\mu$						<b>-0.177</b>
	$\sigma$						
	50%						

TABLE XIII  
DISTRIBUTION RESULTS OF PREDICTION ERRORS IN LIMESTONE CONDITIONS

	CNN	GRU	Transformer	XGBoost	LightGBM	ResCNNGRU	PaHDNN
$F_x$	$\mu$	0.354	-0.632	0.439	-0.266	-0.268	-0.63
	$\sigma$	1.318	1.507	1.119	1.474	1.485	1.688
	50%	0.364	-0.492	0.513	-0.322	-0.399	-0.747
	$\mu$	0.228	0.904	-0.305	0.071	0.142	0.473
$F_z$	$\sigma$	1.037	1.262	0.888	1.045	1.101	1.324
	50%	0.168	0.608	-0.383	0.025	0.161	0.588
	$\mu$	0.25	0.046	<b>-0.002</b>	0.148	0.151	0.149
	$\sigma$	0.672	0.517	0.47	0.47	0.47	-0.01
$M_y$	50%	0.167	-0.006	<b>-0.017</b>	0.096	0.108	0.113
	$\mu$						<b>-0.042</b>
	$\sigma$						
	50%						

TABLE XIV  
DISTRIBUTION RESULTS OF PREDICTION ERRORS IN CORN CONDITIONS

	CNN	GRU	Transformer	XGBoost	LightGBM	ResCNNGRU	PaHDNN
$F_x$	$\mu$	0.392	-0.185	-0.067	-0.371	-0.297	-0.114
	$\sigma$	1.099	1.177	1.025	1.201	1.289	1.08
	50%	0.205	-0.11	-0.079	-0.318	-0.244	-0.057
	$\mu$	-0.1	0.901	0.285	-0.127	0.093	<b>-0.072</b>
$F_z$	$\sigma$	0.776	1.233	0.956	0.659	0.65	0.763
	50%	<b>-0.005</b>	0.847	0.277	0.105	0.186	0.027
	$\mu$	0.199	-0.069	<b>0.061</b>	-0.073	0.083	-0.065
	$\sigma$	0.743	0.438	0.454	0.465	0.421	0.307
$M_y$	50%	0.352	-0.041	0.057	0.056	0.101	-0.055
	$\mu$						<b>-0.011</b>
	$\sigma$						
	50%						

To further validate the generalization ability and accuracy of the proposed network model under unknown working

conditions, an excavation experiment with coal was conducted. A set of simulated data was randomly selected for comparison

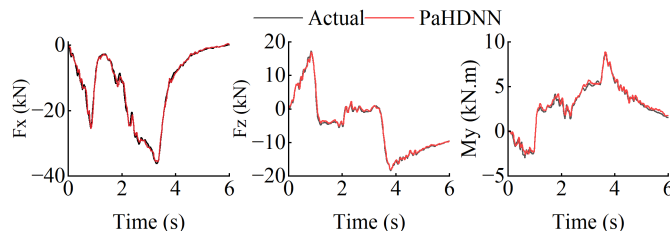


Fig. 19. Prediction results in coal conditions.

TABLE XV

STUDENT'S T-TEST RESULTS, INCLUDING TEST STATISTICS AND  $p$ -VALUES, FOR COMPARING VARIOUS MODELS WITH PaHDNN IN PREDICTING EXCAVATION RESISTANCES

Outputs	Method comparison	Test statistic	P-value
$F_x$	CNN vs. PaHDNN	43.4701	0.00
	GRU vs. PaHDNN	55.8403	0.00
	Transformers vs. PaHDNN	44.2042	0.00
	XGBoost vs. PaHDNN	54.2961	0.00
	LightGBM vs. PaHDNN	54.0247	0.00
	ResCNNGRU vs. PaHDNN	56.2954	0.00
	CNN vs. PaHDNN	43.9991	0.00
	GRU vs. PaHDNN	79.3239	0.00
	Transformers vs. PaHDNN	39.8238	0.00
$F_z$	XGBoost vs. PaHDNN	42.7895	0.00
	LightGBM vs. PaHDNN	39.597	0.00
	ResCNNGRU vs. PaHDNN	53.7496	0.00
	CNN vs. PaHDNN	62.7953	0.00
	GRU vs. PaHDNN	62.8023	0.00
	Transformers vs. PaHDNN	37.4777	0.00
	XGBoost vs. PaHDNN	42.3571	0.00
	LightGBM vs. PaHDNN	30.6451	0.00
	ResCNNGRU vs. PaHDNN	38.1405	0.00
$M_y$	Transformers vs. PaHDNN	37.4777	0.00
	XGBoost vs. PaHDNN	42.3571	0.00
	LightGBM vs. PaHDNN	30.6451	0.00
	ResCNNGRU vs. PaHDNN	38.1405	0.00

between the predicted excavation resistance and the actual values, as shown in Fig. 19. Throughout the entire excavation operation, the PaHDNN network was able to predict excavation resistance with high accuracy.

## VI. CONCLUSION

The autonomous excavation strategy needs to change in real time based on different excavation resistances to ensure optimal excavation efficiency. For the loading operation of loaders, due to the difficulty of directly obtaining the excavating resistance on the actual vehicle, an accurate co-simulation model is constructed to obtain excavating resistance data with similar characteristics to an actual vehicle and then combines with deep learning to achieve real-time and accurate prediction of the excavating resistance. Based on the temporal and spatial variation characteristics of excavation data, GRU and CNN networks are introduced into the PaHDNN network model for feature extraction to determine the time-varying trends of excavation resistance. To alleviate the vanishing gradient problem during deep network training, residual connections are introduced into the CNN network. To verify the effectiveness, generality, and superiority of the proposed model, datasets are constructed for different working conditions using the simulated shovel loading data and compared with the traditional network methods.

It is important to highlight that our proposed solution rectifies the prior issue of poor prediction performance from neural networks, which stemmed from the oversight of spatial local features in the resistance sequence. The dataset

developed in this article is derived from a robust simulation model. This poses a problem for the transferability of different loader types with differing dynamic properties. In real-world engineering, limitations can also come from limited computing power in industrial control systems, latency, and other factors. Therefore, in future work, we can consider introducing transfer learning and further optimizing the network structure to enhance the model's applicability and efficiency in applications.

## REFERENCES

- [1] J. Lu, Q. Bi, Y. Li, and X. Li, "Estimation of fill factor for Earth-moving machines based on 3D point clouds," *Measurement*, vol. 165, Dec. 2020, Art. no. 108114.
- [2] T. Li, Z. Ren, X. Pang, D. Chen, and S. Cao, "Dynamic digging force modeling and comparative analysis of backhoe hydraulic excavators," *Meas. Sci. Technol.*, vol. 35, no. 3, Dec. 2023, Art. no. 035025.
- [3] J. Yao et al., "Bucket loading trajectory optimization for the automated wheel loader," *IEEE Trans. Veh. Technol.*, vol. 72, no. 6, pp. 6948–6958, Jun. 2023.
- [4] T. Zhang, T. Fu, T. Ni, H. Yue, Y. Wang, and X. Song, "Data-driven excavation trajectory planning for unmanned mining excavator," *Autom. Construct.*, vol. 162, Jun. 2024, Art. no. 105395.
- [5] S. Zhou et al., "A load forecasting framework considering hybrid ensemble deep learning with two-stage load decomposition," *IEEE Trans. Ind. Appl.*, vol. 60, no. 3, pp. 4568–4582, May 2024.
- [6] Y. Zhao, J. Wang, Y. Zhang, and C. Luo, "A novel method of soil parameter identification and force prediction for automatic excavation," *IEEE Access*, vol. 8, pp. 11197–11207, 2020.
- [7] R. Madau, D. Colombara, A. Alexander, A. Vacca, and L. Mazza, "An online estimation algorithm to predict external forces acting on a front-end loader," *Proc. Inst. Mech. Eng., I. J. Syst. Control Eng.*, vol. 235, no. 9, pp. 1678–1697, Oct. 2021.
- [8] Q. Bi, G. Wang, R. Yang, Y. Liu, Y. Lu, and S. Xing, "Study on theory and methods of payload online estimation for cable shovels," *J. Brazilian Soc. Mech. Sci. Eng.*, vol. 41, no. 1, pp. 1–13, Jan. 2019.
- [9] S. Wang, Y. Yin, Y. Wu, and L. Hou, "Modeling and verification of an acquisition strategy for wheel loader's working trajectories and resistance," *Sensors*, vol. 22, no. 16, Aug. 2022, Art. no. 5993.
- [10] G. Gao, J. Wang, T. Ma, Y. Han, X. Yang, and X. Li, "Optimisation strategy of torque distribution for the distributed drive electric wheel loader based on the estimated shovelling load," *Vehicle Syst. Dyn.*, vol. 60, no. 6, pp. 2036–2054, Jun. 2022.
- [11] J. Wei, J. Zhao, and J. Wang, "Research on shovel-force prediction and power-matching optimization of a large-tonnage electric wheel loader," *Appl. Sci.*, vol. 13, no. 24, Dec. 2023, Art. no. 13324.
- [12] S. Li, S. Wang, X. Chen, G. Zhou, B. Wu, and L. Hou, "Application of physics-informed machine learning for excavator working resistance modeling," *Mech. Syst. Signal Process.*, vol. 209, Mar. 2024, Art. no. 111117.
- [13] Y. Shen, J. Wang, C. Feng, Q. Wang, and J. Fan, "Data-physics hybrid-driven external forces estimation method on excavators," *Mech. Syst. Signal Process.*, vol. 223, Jan. 2025, Art. no. 111902.
- [14] B. Wu, L. Hou, S. Wang, Y. Yin, and S. Yu, "Predictive modeling of loader's working resistance measurement based on multi-sourced parameter data," *Autom. Construct.*, vol. 149, May 2023, Art. no. 104805.
- [15] D. Huo, J. Chen, H. Zhang, Y. Shi, and T. Wang, "Intelligent prediction for digging load of hydraulic excavators based on RBF neural network," *Measurement*, vol. 206, Jan. 2023, Art. no. 112210.
- [16] Y. Chen, G. Shi, H. Jiang, and T. Zheng, "Research on the prediction of insertion resistance of wheel loader based on PSO-LSTM," *Appl. Sci.*, vol. 13, no. 3, p. 1372, Jan. 2023.
- [17] G. Hua, S. Wang, M. Xiao, and S. Hu, "Research on the uplift pressure prediction of concrete dams based on the CNN-GRU model," *Water*, vol. 15, no. 2, p. 319, Jan. 2023.
- [18] K. He, X. Zhang, S. Ren, and J. Sun, "Deep residual learning for image recognition," in *Proc. IEEE Conf. Comput. Vis. Pattern Recognit. (CVPR)*, Jun. 2016, pp. 770–778.
- [19] F. Harrou, A. Zeroual, F. Kadri, and Y. Sun, "Enhancing road traffic flow prediction with improved deep learning using wavelet transforms," *Results Eng.*, vol. 23, Sep. 2024, Art. no. 102342.

- [20] M. M. Hittawe, F. Harrou, M. A. Togou, Y. Sun, and O. Knio, "Time-series weather prediction in the red sea using ensemble transformers," *Appl. Soft Comput.*, vol. 164, Oct. 2024, Art. no. 111926.
- [21] Z. Liu, W. Wu, J. Li, C. Zheng, and G. Wang, "Dynamic inclination identification methods for mine-use monorail crane transport robots under dual operating conditions," *IEEE Sensors J.*, vol. 24, no. 21, pp. 35939–35953, Nov. 2024.
- [22] C. Sun, Y. Zhang, Y. Zhang, H. Zhao, H. Guo, and X. Hao, "A soft sensor model for predicting cement-specific surface area based on convolution fast recurrent unit network," *IEEE Sensors J.*, vol. 23, no. 1, pp. 425–433, Jan. 2023.
- [23] W. Bai, G. Zheng, Y. Mu, H. Ma, Z. Han, and Y. Xue, "Cooperative spectrum sensing method based on channel attention and parallel CNN-LSTM," *Digit. Signal Process.*, vol. 158, Mar. 2025, Art. no. 104963.
- [24] J. Li, C. Chen, Y. Li, H. Wu, and X. Li, "Difficulty assessment of shoveling stacked materials based on the fusion of neural network and radar chart information," *Autom. Construct.*, vol. 132, Dec. 2021, Art. no. 103966.
- [25] H. Lee, M. Kim, and W. Yoo, "Force-balancing algorithm to remove the discontinuity in soil force during wheel loader excavation," *J. Mech. Sci. Technol.*, vol. 32, no. 10, pp. 4951–4957, Oct. 2018.
- [26] J. Maciejewski, A. Jarzębowski, and W. Trąmpczyński, "Study on the efficiency of the digging process using the model of excavator bucket," *J. Terramech.*, vol. 40, no. 4, pp. 221–233, Oct. 2003.
- [27] S. Sarata, Y. Weeramhaeng, and T. Tsubouchi, "Approach path generation to scooping position for wheel loader," in *Proc. IEEE Int. Conf. Robot. Autom.*, Aug. 2005, pp. 1809–1814.
- [28] O. Azulay and A. Shapiro, "Wheel loader scooping controller using deep reinforcement learning," *IEEE Access*, vol. 9, pp. 24145–24154, 2021.
- [29] S. Dadhich, F. Sandin, U. Bodin, U. Andersson, and T. Martinsson, "Adaptation of a wheel loader automatic bucket filling neural network using reinforcement learning," in *Proc. Int. Joint Conf. Neural Netw. (IJCNN)*, Jul. 2020, pp. 1–9.
- [30] D. N. Reshef et al., "Detecting novel associations in large data sets," *Science*, vol. 334, no. 6062, pp. 1518–1524, Dec. 2011.
- [31] W. Shaojie, H. Liang, J. Lee, and B. Xiangjian, "Evaluating wheel loader operating conditions based on radar chart," *Autom. Construct.*, vol. 84, pp. 42–49, Dec. 2017.
- [32] H. Wu et al., "The improved wavelet denoising scheme based on robust principal component analysis for distributed fiber acoustic sensor," *IEEE Sensors J.*, vol. 23, no. 19, pp. 22944–22951, Oct. 2023.
- [33] I. F. Kilincer, F. Ertam, and A. Sengur, "Machine learning methods for cyber security intrusion detection: Datasets and comparative study," *Comput. Netw.*, vol. 188, Apr. 2021, Art. no. 107840.
- [34] W. H. Chung, Y. H. Gu, and S. J. Yoo, "CHP engine anomaly detection based on parallel CNN-LSTM with residual blocks and attention," *Sensors*, vol. 23, no. 21, p. 8746, Oct. 2023.
- [35] R. Wang, Q. Song, Y. Peng, P. Jin, Z. Liu, and Z. Liu, "A milling tool wear monitoring method with sensing generalization capability," *J. Manuf. Syst.*, vol. 68, pp. 25–41, Jun. 2023.
- [36] C. Qin et al., "Precise cutterhead torque prediction for shield tunneling machines using a novel hybrid deep neural network," *Mech. Syst. Signal Process.*, vol. 151, Apr. 2021, Art. no. 107386.
- [37] M. A. P. Putra, A. P. Hermawan, D.-S. Kim, and J.-M. Lee, "Data prediction-based energy-efficient architecture for industrial IoT," *IEEE Sensors J.*, vol. 23, no. 14, pp. 15856–15866, Jul. 2023.



**Shunshun Zhang** was born in Henan, China, in 1994. He received the B.S. degree in mechanical engineering from Shenyang Jianzhu University, Shenyang, China, in 2022. He is currently pursuing the M.E. degree with the School of Mechanical and Aerospace Engineering, Jilin University, Changchun, China.

His main research interests include hydraulic system modeling for loader work units and hydraulic system control for construction vehicles.



**Guanlong Chen** was born in Nei Mongol, China, in 1998. He received the B.S. degree in mechanical engineering from Jilin University, Changchun, China, in 2020, where he is currently pursuing the Ph.D. degree.

His main research interests include autonomous shoveling operations of loaders, simulation modeling of complete vehicle systems, and material sensing and recognition.



**Zongwei Yao** received the B.Sc. and Ph.D. degrees in engineering from Jilin University, Changchun, China, in 2008 and 2013, respectively.

He is currently a Professor with Jilin University, where he is heading a group working on intelligent engineering vehicles. He has been focusing on research areas of 3-D construction of the environment, autonomous operation of construction vehicles, and mechanical system dynamics.



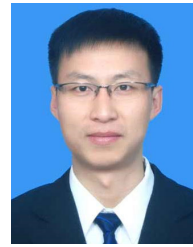
**Qiushi Bi** received the B.S. degree in agricultural mechanization and automation from Northwest A&F University, Xianyang, China, in 2011, and the M.S. and Ph.D. degrees in mechanical design and theory from Jilin University, Changchun, Jilin, China, in 2014 and 2019, respectively.

He is currently an Associate Professor with the School of Mechanical and Aerospace Engineering, Jilin University. His main research directions are mining equipment autonomous shoveling, autonomous walking, autonomous loading, and unloading; nonstructural environment air-ground cooperative whole-area information sensing; purely electric-driven engineering equipment multicoupling simulation and intelligent control; and multidisciplinary optimization of large-scale mining crushing and milling equipment.



**Yingnan Li** (Student Member, IEEE) was born in Jilin, China, in 1996. He received the B.S. degree in weapons launch engineering from Nanjing University of Science and Technology, Nanjing, China, in 2018.

He is currently working toward the master's degree in mechanical engineering with the School of Mechanical and Aerospace Engineering, Jilin University, Changchun, China. His current research interests include autonomous operating systems for construction vehicles, longitudinal and transverse tracking control of loaders, and electrohydraulic servo control of work devices.



**Xuefei Li** was born in Gansu, China, in 1986. He received the B.S. degree in mechanical engineering and the Ph.D. degree in mechanical design and theory from Jilin University, Changchun, Jilin, China, in 2009 and 2014, respectively.

He is currently a Professor with the School of Mechanical and Aerospace Engineering, Jilin University. His research interests include driverless and intelligent operation technology for engineering vehicles, robot navigation, path planning and trajectory tracking control, and intelligent agricultural machinery.